Drying dip-coated colloidal films

Joaquim Li,[1] Bernard Cabane,[2] Michael Sztucki,[2] Jérémie Gummel,[2] and Lucas Goehring[3,*]

[1]*PMMH, CNRS UMR 7636, ESPCI, 10 rue Vauquelin, 75231 Paris Cedex 05, France*
[2]*ESRF, B.P. 220, 38043 Grenoble, France*
[3]*Max Planck Institute for Dynamics and Self-Organization, Bunsenstraße 10, D37073 Göttingen, Germany*

(Dated: September 10, 2011)

We present the results from a Small Angle X-ray Scattering (SAXS) study of lateral drying in thin films. The films, initially 10 μm thick, are cast by dip-coating a mica sheet in an aqueous silica dispersion (particle radius 8 nm, volume fraction $\phi_s = 0.14$). During evaporation, a drying front sweeps across the film. An X-ray beam is focused on a selected spot of the film, and SAXS patterns are recorded at regular time intervals. As the film evaporates, SAXS spectra measure the ordering of particles, their volume fraction, the film thickness and the water content, and a video camera images the solid regions of the film, recognized through their scattering of light. We find that the colloidal dispersion is first concentrated to $\phi_s = 0.3$, where the silica particles form a gel with repulsive interactions. Then the particles aggregate until they form a cohesive wet solid at $\phi_s = 0.68 \pm 0.02$. Further evaporation from the wet solid leads to evacuation of water from pores of the film, but leaves a residual water fraction $\phi_w = 0.16$. The whole drying process is completed within three minutes. An important finding is that, in any spot (away from boundaries), the number of particles is conserved throughout this drying process, leading to the formation of a homogeneous deposit. This implies that no flow of particles occurs in our films during drying, a behavior distinct to that encountered in the iconic coffee-stain drying. It is argued that this type of evolution is associated with the formation of a transition region that propagates ahead of the drying front. In this region the gradient of osmotic pressure balances the drag force exerted on the particles by capillary flow toward the liquid-solid front.

INTRODUCTION

Coatings are often made through deposition of liquid colloidal dispersions. Common examples are paints, anti-corrosion coatings and ceramic coatings. In most cases, the dispersion is applied as a liquid film, and it changes into a solid film as a result of solvent evaporation. A variety of deposition patterns can be obtained, depending on the evaporation profile over the liquid film and on the flows taking place inside the deposit during drying [1–7]. The two extreme situations are as follows:

(a) Homogeneous film formation: in the simplest case, there is no lateral flow through the liquid film, and all volatile components are evaporated locally. The number of particles at each point of the film is conserved throughout the drying process. Therefore the deposition of a uniform liquid colloidal film leads to a final solid film that has homogeneous composition, thickness and microstructure. Relatively homogeneous films can also be obtained through mechanisms where there is a moving liquid-solid boundary, and there is a flow of liquid phase near this boundary [8, 9].

(b) Coffee-ring: this process has also been extensively studied [1, 2]. In this situation a macroscopic flow throughout the liquid carries nearly all the particles to the fixed edges of the film, where they pack into a dense rim. At the end of drying, no film is left in between these outer rims. Other situations where there are macroscopic flows have given rise to original ways of shaping deposits [4, 5, 10, 11].

Strangely, we do not have a simple rule to predict which colloidal films will yield a uniform solid film, and which ones will evolve through the coffee-ring effect, where a flow carries the particles to the rims. To some extent, this shortcoming originates from the fact that we do not have sufficient insight into the phenomena that take place in the liquid regions of the film, for instance on the changes in film height, particle concentration and microstructure at every spot in the film, during evaporation.

Previous work has provided a robust description of the film formation processes during lateral drying [3, 4, 9, 12, 13]. The general observation is that drying fronts sweep across the liquid film, starting from the edge and progressing toward the middle. Modeling of these drying fronts has suggested that 3 distinct transitions take place: an ordering transition where the particles reach maximum order, an aggregation transition where they form irreversible bonds with each other, so that the film becomes a solid, and a de-wetting transition where the pores within the film are evacuated (Fig. 1). Local flows near the liquid-solid transition have been observed, however there is little information on far-field flows that would take place away from these fronts. Moreover, other than one publication on latex dispersions [14], there is a lack of quantitative information on such basic features as the volume fraction of particles at various distances from the drying fronts.

Here we report the results of experiments that were designed to provide microscopic information in the liquid regions of the film, before the liquid-solid transition. Specifically, we studied the evolution upon drying of con-

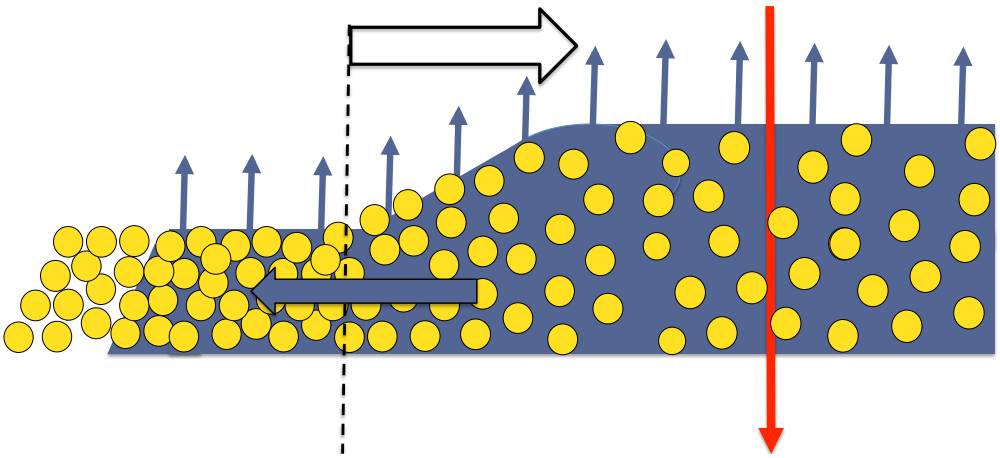

FIG. 1: A liquid colloidal dispersion (right) dries to form a solid film (left). Evaporation from the surface of the liquid and from that of the wet solid drive a drying front that sweeps across the film (white arrow). Some liquid flows into the wet solid (dark horizontal arrow). The thickness, composition, and microstructure at one location in the film are investigated through scattering from a synchrotron beam of X-rays (red arrow), as the front advances across the fixed beam.

centrated aqueous dispersions of nanometric silica particles. We deposited very thin films (initially 10 μm thick, drying to 2 μm thick) of these dispersions through dip-coating onto flat vertical substrates that were fully wetted by the liquid. Then we used Small Angle X-ray Scattering (SAXS) to determine the microscopic state, the composition and the thickness of the film at the spot irradiated by the beam, throughout the whole evaporation process. The results show that the model of directional drying can successfully be applied to films in this thin limit, and provide some answers to the following questions:

(1) Are there significant flows of the liquid phase, either in the vicinity of the liquid solid front, or at large distances from it (i.e."far-field flows")?

(2) Are the particles carried by such flows, do they remain in their original location throughout the drying process, or do they accumulate at the liquid-solid boundary?

(3) What is the volume fraction of particles ahead of the front where the liquid-solid transition takes place?

(4) How and when does the liquid-solid transition take place, and what are the volume fraction and the structure of the resulting solid phase?

(5) Is the evaporation rate over the wet solid film the same as the evaporation rate over the liquid dispersion?

Here we show that the SAXS technique can provide direct answers to questions (1), (3) and (4), and indirect answers to (2) and (5) through simple modeling of the transport processes. We show that these answers characterize the drying process in the case of homogeneous film formation. We then examine whether similar information on different films could make it possible to predict the height profile of dried colloidal films.

MATERIALS AND METHODS

Aqueous dispersions of colloidal silica (Ludox® HS-40, Sigma-Aldrich) were used throughout. They were filtered to 0.2 μm (polyethersulfone membrane, VWR) and dialysed for three days against an aqueous solution of 5 mM NaCl at pH 9. The washed silica dispersions were then concentrated by further dialysis against aqueous solutions of PEG 35000 (Aldrich) at pH 9 and 5 mM NaCl. Osmotic equilibrium was reached after 20 days [15]. A sample of each dispersion was weighed, oven-dried, and reweighed to measure the silica volume fraction ϕ_s. A set of dispersions was thus produced, with ϕ_s between 0.04 and 0.43 depending on the concentration of PEG used. The dispersion with $\phi_s = 0.14$ was used for coating experiments; all others were used for calibration.

Colloidal films were produced using the dip-coating technique (Fig. 2). A thin sheet of mica (40 × 30 × 0.05 mm) cleaned by water, ethanol, acetone and a butane torch, was placed in the path of the X-ray beam. One side of this sheet was covered with hydrophobic adhesive tape in order to prevent film deposition on that side. The colloidal silica dispersions wet the mica but not the hydrophobic tape. A tank filled with dispersion was raised so that the mica sheet was immersed to a depth of 15-20 mm. The tank was then lowered at a constant velocity of 470 μm/s to just below the lower edge of the mica, depositing a film on the mica. At this drawing velocity, films with an initial thickness of 10 μm were obtained. Optical observation of the dried films showed that their thickness was uniform across the film, except for the outer edges where small rims had formed.

The film was illuminated with a white lamp, and a video camera gathered the light reflected by its surface; images were recorded during film deposition and evapo-

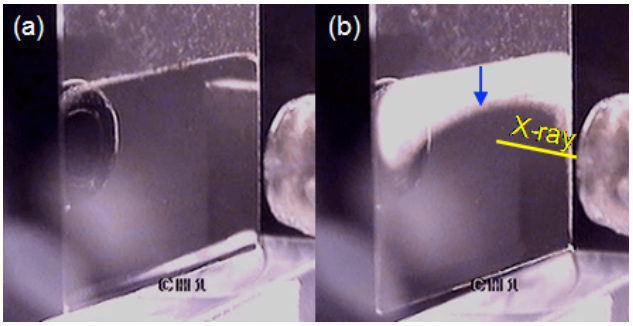

FIG. 2: Experimental setup and visualisation, showing the mica sheet, 30 mm wide, (a) just after film deposition and (b) 60 s later. Lateral drying occurred with a drying front moving from the top of the sheet to the bottom (white band and blue arrow). X-rays are projected from the metallic cylinder seen on the right. A reflected image of this cylinder can be seen on the film. The reservoir used to dip-coat the sheet is seen at the bottom of the image.

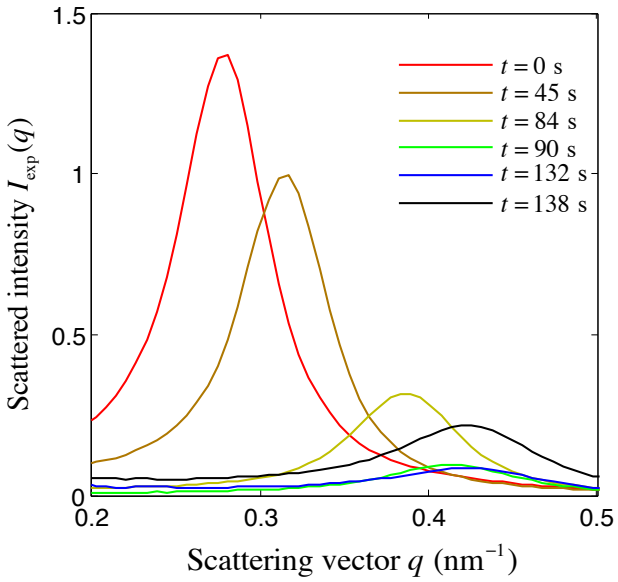

FIG. 3: Intensity of X-rays scattered from one point in the film, during the course of drying. From t = 0 to 90 s, the peak position gradually shifts to higher q values, as the particle volume fraction increases. At the same time the peak intensity drops. At t = 90 s the peak position is fixed, as the particle volume fraction reaches its upper limit. For a time (t = 90 to 132 s) the compact film remains saturated with fluid, and the peak intensity remains constant. Finally, however, the film loses water (t = 132 to 138 s), the scattering contrast between the silica and the pores increases, and the signal rises.

ration, as shown in Fig. 2. Lateral drying occurred with a visibly white drying front moving from the top of the film to the bottom.

The relative positions of the X-ray beam and the sheet of mica were such that the beam passed through the deposited film. SAXS acquisition began immediately after the dispersion tank was stopped. During drying, spectra were recorded every 3 s, recording the structural evolution of the film at one fixed point while the drying front approached and crossed the beam position. In the following, time $t = 0$ is defined as the time of the first recorded spectrum.

SAXS measurements were done using the ID02 instrument at the European Synchrotron Radiation Facility in Grenoble, France. The detector was a CCD camera (FReLoN 4M) with 2048 × 2048 pixels and 10 × 10 cm area. The beam cross-section was an ellipse with dimensions (full width at half maximum) of 0.07 mm in the vertical direction and 0.25 mm in the horizontal direction. The sample to detector distance was 1 m and the wavelength of the X-rays was 0.1 nm, giving a q-range extending from 0.1 nm^{-1} to 4 nm^{-1}. All measurements were done under atmospheric pressure, at room temperature and in ambient humidity.

During acquisition, standard corrections for X-ray beam transmission and flux, detector efficiency and distortion were applied to the recorded CCD image. SAXS 2-D images were then collapsed by azimuthal regrouping, while applying a mask to remove faulty regions of the images, mainly due to the beam stop. The background scattering from the mica sheet before film deposition was subtracted from the intensity curves. This yielded curves of intensity $I_{exp}(q)$ vs. scattering vector q. If the sample thickness h was known, division by h would yield the intensity on an absolute scale, $I_{abs}(q)$:

$$I_{abs}(q) = I_{exp}(q)/h \quad (1)$$

In the present case, however, we report values of $I_{exp}(q)$ and use them to deduce the film thickness h.

Small angle scattering by the films is produced by the differences in electron densities between silica, water and air. We used densities of 602 e/nm^3 for silica, 334 e/nm^3 for water and 0 e/nm^3 for air. Multiplying by the scattering length of the electron, 2.82×10^{-15} m yields the densities of scattering length $\rho_s = 1.70 \times 10^{15}$ m^{-2} for silica, $\rho_w = 0.94 \times 10^{15}$ m^{-2} for water, and $\rho_0 = 0$ m^{-2} for air.

RESULTS

Evolution of the scattered intensity during drying

Selected SAXS spectra from a typical drying sequence are shown in Fig. 3. The main peak changes in position and intensity over the course of drying. Initially moving to higher q values, the peak position becomes fixed at t = 90 s. Then, between t = 132 and 138 s, there is an

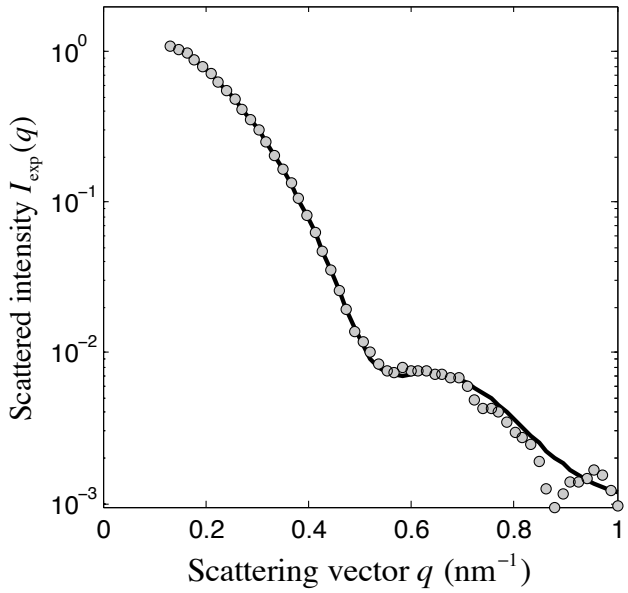

FIG. 4: Scattered intensity (circles) of a dispersion of Ludox HS-40 diluted to a silica volume fraction $\phi_s = 0.001$. The solid line is a fit to the theoretical scattering by a dispersion of homogeneous spheres with a Schultz distribution of radii with average radius $R_p = 8.15$ nm and width $\sigma_R/R_p = 0.14$.

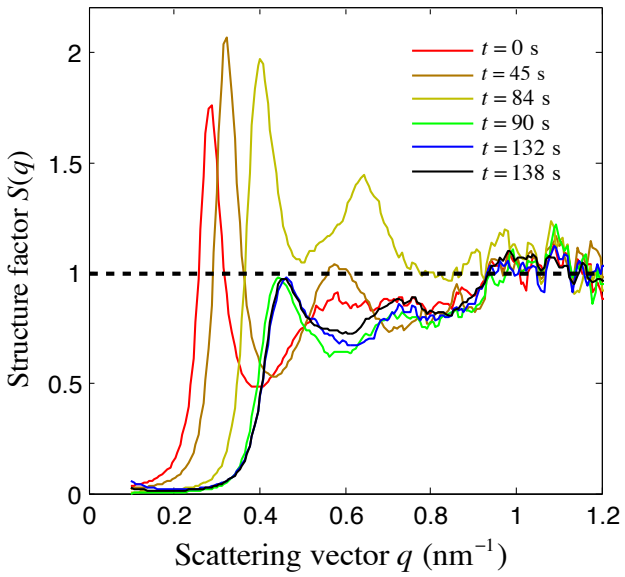

FIG. 5: Structure factors of a drying film, calculated as the renormalized ratio of the scattered intensity (Fig. 3) to the form factor fitted to a dilute dispersion (Fig. 4). The shape of the main peak reflects the quality of the ordering of the particles. The position of the main peak is related to the average nearest-neighbour distance of the particles. Note the large change in peak height between $t = 84$ and 90 s, caused by the aggregation of the particles at the liquid-solid transition, and the absence of structural changes in the solid, after $t = 90$ s.

increase of the peak intensity, but its position remains locked at the same q value. Finally, after $t = 138$ s, both the intensity and position of the peak remain constant.

Structure factors

The intensity scattered by a dispersion depends on the sizes, shapes and relative positions of its particles. For a dispersion of identical spherical particles, the intensity $I_{exp}(q)$ is the product of a form factor $P(q)$ that expresses the interferences between rays scattered by different atoms within a particle, and a structure factor $S(q)$ that measures the correlations between the positions of the particles [16, 17]:

$$I_{exp}(q) = h\phi_s V_p(\rho_s - \rho_w)^2 P(q)S(q) \qquad (2)$$

where h is the film thickness, ϕ_s is the volume fraction of particles in the dispersion, V_p is the particle volume, and ρ_s and ρ_w are the densities of scattering length of silica and water.

The structure factor $S(q)$ is related to the pair correlation function $g(r)$ of inter-particle distances r by

$$S(q) = 1 + \frac{\phi_s}{V_p}\int_0^\infty (g(r) - 1)\frac{\sin(qr)}{qr} 4\pi r^2 dr \qquad (3)$$

In the case of spherical particles of radius R_p, the form factor $P(q)$ is

$$P(q) = 9\left[\frac{\sin(qR_p) - qR_p\cos(qR_p)}{(qR_p)^3}\right]^2 \qquad (4)$$

When the particles are polydisperse in radii, it is customary to include all effects of polydispersity in $P(q)$, which is then obtained from the scattering of a dilute dispersion. Fig. 4 shows the measured scattering from a very dilute dispersion ($\phi_s = 0.001$) and a fit to the theoretical form factor $P(q)$ of a dispersion of homogenous spheres with a Schulz distribution for the radii [16].

The classical procedure is to now define the effective structure factor as the ratio of the intensity to $P(q)$ [16, 17]. We used the model form factor $P(q)$ shown in Fig. 4 for all spectra, and extracted $S(q)$ from Eqn. (2), invoking the condition that $S(q) \to 1$ at large q values, as indicated by Eqn. (3). Fig. 5 shows the resulting structure factors corresponding to the spectra shown in Fig. 3. They have a primary peak whose position is related to the average nearest-neighbour distance of the particles, and whose shape reflects the ordering of the particles under the effect of their ionic repulsions.

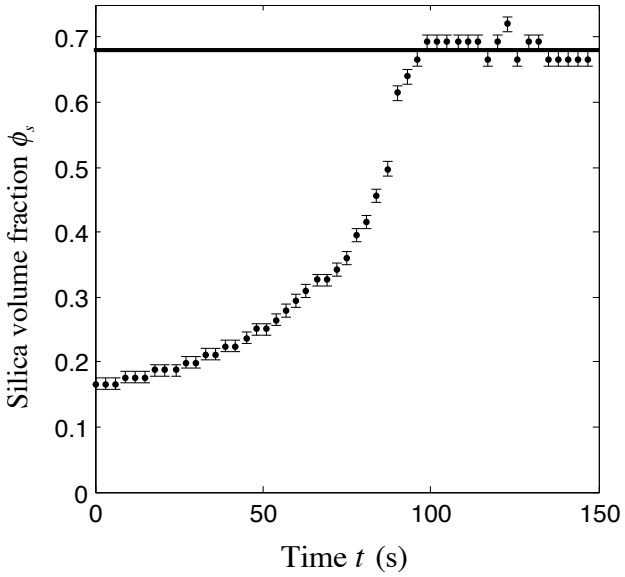

FIG. 6: The volume fraction of silica particles rises during the drying of the film. After t = 93 s, the constant volume fraction is that of the aggregated solid. The horizontal line shows the final volume fraction $\phi_f = 0.68$.

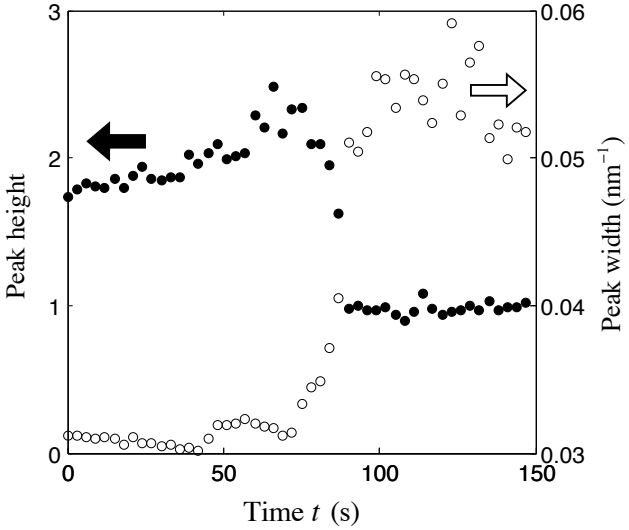

FIG. 7: Peak height (filled circles) and half-width-half-maximum (open circles) of the primary peak of the structure factor. The initial rise in peak height reflects ordering due to the ionic repulsions between particles, whereas the drop starting at t = 72 s indicates a decrease in short-range order, caused by the onset of aggregation.

Changes in peak position, width, and height

The position of the primary peak of the structure factor, q_{peak}, is related to the local silica volume fraction ϕ_s. Using calibration standards of known ϕ_s we found good agreement with the law expected for a face-centred cubic structure [18–20] (see Supplemental Information)

$$(q_{peak})^3 = \frac{36\pi^2\sqrt{3}}{(2R_p)^3}\phi_s \qquad (5)$$

Through this relation, we calculated how the silica volume fraction ϕ_s, at the location irradiated by the beam, evolved over time (Fig. 6). During the course of drying, this volume fraction rose progressively until t = 93 s. After this time ϕ_s did not change, to within experimental resolution; an average value of $\phi_s = 0.68 \pm 0.02$ was found, for all data from t = 96 s onward. The change from increasing volume fraction to constant volume fraction is indicative of an aggregation or solidification transition that was complete by $t = 93 \pm 3$ s.

The height S_{max} of the first peak of the structure factor reflects the order of the silica particles. For concentrated colloidal dispersions of repelling particles, S_{max} is usually between 1.5 and 2.8 [21–25]. For the drying film, between times t = 0 and 72 s, S_{max} rose slowly from 1.9 to 2.3, indicating that the short range order was indeed caused by interparticle repulsions, and that this order increased as the dispersion was concentrated by evaporation (Fig. 7). However, between t = 72 s and t = 90 s, the main peak collapsed rapidly to $S_{max} = 1$. This drop was associated with a rapid increase in the peak width, determined as the half-width at half-maximum on the low-q side of the main peak. Both changes indicate a loss of short-range order [21–27]. After t = 90 s, the peak height stayed constant at $S_{max} = 1$ (Fig. 5), which is much lower than a liquid structure peak at this volume fraction, and the width of the peak also stabilized. The stabilization after t = 90 s, and the simultaneous fixing of the volume fraction (as shown in Fig. 6) both suggest that an irreversible process was completed by this time.

According to these changes in the position, width and height of the peak in $S(q)$, the film passed through three distinct stages. Until t = 72 s and $\phi_s = 0.35$, the compaction caused by evaporation caused the interparticle order to increase continuously. After t = 72 s the compaction continued but was now associated with a rapid decrease in order that may reflect jamming [27] or limited aggregation of the particles [26, 28]. The second transition arrived at t = 90 s and $\phi_s = 0.61$. It produced a stabilization of short-range order and volume fraction, which was complete at $\phi_s = 0.68$. The stabilization of order reflects the end of the aggregation process and that of ϕ_s indicates maximal compaction of the silica particles. These three stages match the macroscopic properties of dispersions that were concentrated through osmotic stress, which were liquid before $\phi_s = 0.35$, gel-like beyond 0.35, and solid at volume fractions beyond 0.5.

High-q limit of the scattered intensity

The high-q part of the scattering can also be used to extract information regarding the content of the film at the location irradiated by the beam. For a system with only two levels of scattering density, the high-q limit of the scattering obeys Porods law [16, 17]

$$\lim_{q\to\infty} q^4 I_{exp}(q) = 2\pi h \Delta\rho^2 \frac{A}{V} \tag{6}$$

where A is the total area of interface in the volume V of film that is irradiated by the beam, moreover, here the contrast $\Delta\rho^2 = (\rho_s - \rho_w)^2 = 5.69 \times 10^{29}$ m^{-4}.

Since V varies as $1/h$ (the beam cross-section being constant), this limit gives access to A. Porods law does not depend on any assumptions regarding the organization of the particles. The only assumption is that there are only two levels of electronic density, i.e. that the particles are immersed in a homogeneous aqueous phase. This is the case for a liquid film or for a wet solid film. Moreover, Eqn. (6) can be rewritten so that it does not depend on the beam dimensions:

$$\lim_{q\to\infty} q^4 I_{exp}(q) = 2\pi h \phi_s \Delta\rho^2 \frac{A_p}{V_p} \tag{7}$$

where A_p is the surface area of one particle and V_p its volume. The quantity $h\phi_s$ now appears here, which is the solid content at the location irradiated by the beam. We measured the Porod limit by plotting I_{exp} vs. q^{-4} and fitting the beginning of this curve with a linear function, whose slope is the Porod limit. Due to the low signal/noise ratio at high q, these fits were done over a q range that extended from 1.2 to 4 nm^{-1}. We note that even though this method is precise, the restriction of range leads us to systematically under-measure the limit; according to fits of the spectra of bulk dispersions, where the signal/noise ratio is better, the Porod limits measured for the films are consistently 80 % of the true asymptotic values (Supplemental Information).

Fig. 8 presents the variation in the Porod limit throughout the drying process. Surprisingly, it remains constant for the first 130 s of drying. Accordingly, the number of particles at the spot irradiated by the beam was conserved through all these stages of drying.

At $t = 130$ s the Porod limit of the scattered intensity rises abruptly to approximately three times its initial value. Since the film was in a solid state at this time, particles can no longer move or accumulate. Therefore, this rise must be caused by a change in $\Delta\rho^2$, indicating that water is evacuated from the pores of the wet solid film. Beyond this point the film is a system with three levels of scattering density, which we shall describe shortly.

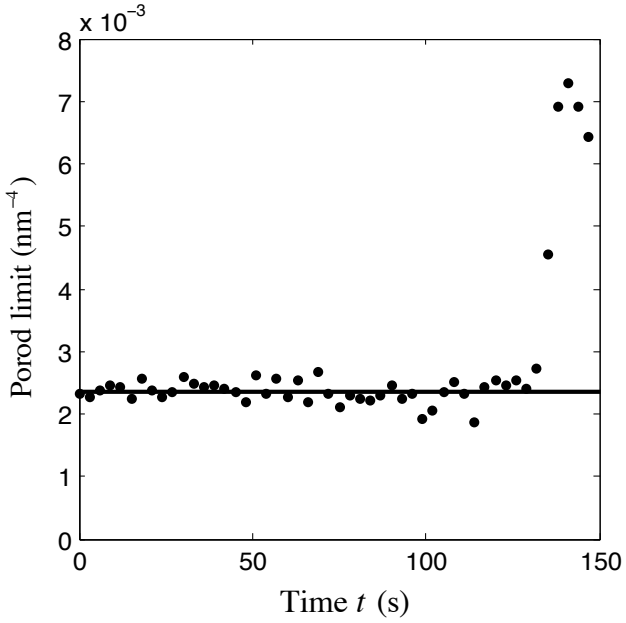

FIG. 8: Variation of the Porod limit of the scattered intensity during drying. The constant value up to $t = 130$ s indicates that the number of particles at the spot irradiated by the beam was constant, and that they remained immersed in water. The jump at $t = 130$ s is interpreted as an increase in contrast, resulting from the intrusion of air into the pore spaces of the film. The horizontal line is traced at the average value of the Porod limit for the liquid film.

Integral of the scattered intensity

Further evidence of the conservation of the number of particles in the irradiated volume was obtained by considering the integral of the intensity over all scattering vectors, also called the invariant, Q [16, 17]:

$$Q = \int_0^\infty I_{abs}(q) q^2 dq = 2\pi^2 \langle\eta^2\rangle \tag{8}$$

where $I_{abs}(q)$ is the scattered intensity per unit volume, as defined in Eqn. (1), and $\langle\eta^2\rangle$ is the average fluctuation of the density of scattering length within the irradiated volume. For a sample of thickness h with only two levels of density of scattering length, ρ_s and ρ_w, the integral of the measured intensity $I_{exp} = hI_{abs}$ is

$$Qh = \int_0^\infty I_{exp}(q) q^2 dq = 2\pi^2 h \langle\eta^2\rangle = 2\pi^2 \Delta\rho^2 h \phi_s (1 - \phi_s) \tag{9}$$

Thus, if the solid content at the location irradiated by the beam is constant, then Qh should vary as the water content of the film:

$$Qh = K(1 - \phi_s) \tag{10}$$

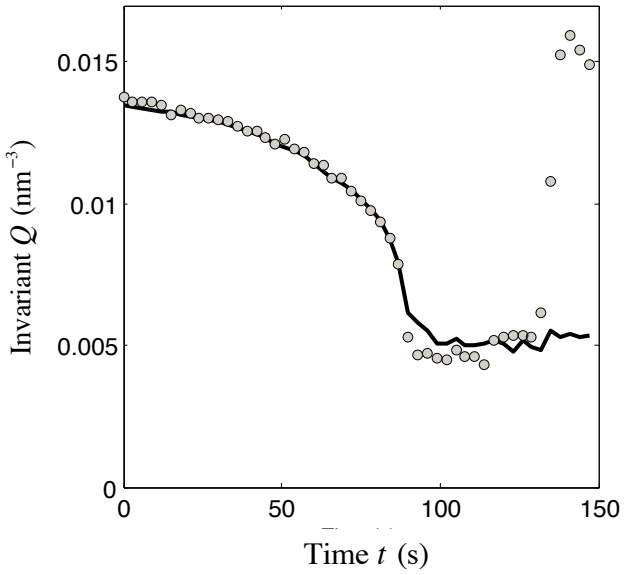

FIG. 9: Changes in the invariant Q of the scattered intensity during drying. During the first 90 seconds, changes in the magnitude reflect a dependence of the invariant on the water volume fraction in the film. The flat section between $t = 90$ s and $t = 130$ s corresponds to a period of time during which the film is in the wet solid state. The sudden jump in magnitude at $t = 130$ s corresponds to the dewetting transition, as the integral is also relative to the contrast in the density of scattering length. The line gives the expected Q, calculated from the volume fraction data in Fig. 6 and the Porod limit presented in Fig. 8.

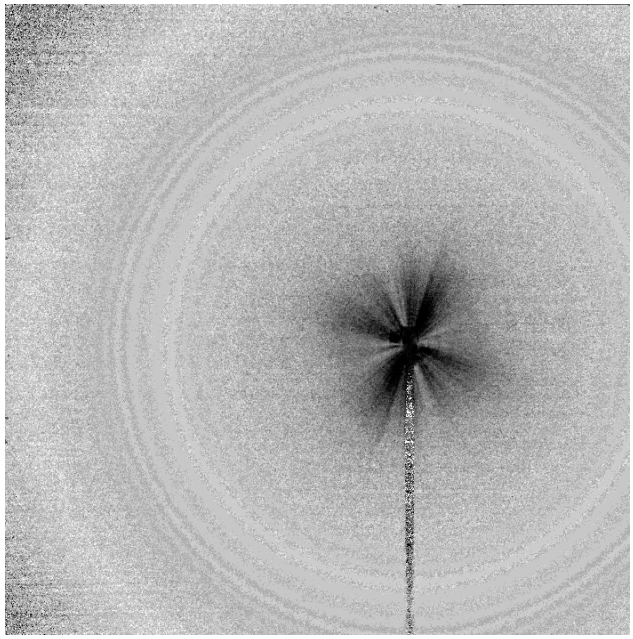

FIG. 10: Anisotropic scattering from cracks. Shown is the difference between two 2D spectra, captured 3 s apart, which highlights the sudden appearance of low-q structures. At this time the silica volume fraction becomes fixed, and the camera shows a decrease in the transparency of the film. The rings originate from the short-range order of silica particles. The streaks in the centre of the image, next to the beam-stop, are interpreted as scattering from cracks.

with K a constant. Fig. 9 shows the evolution of Q as well as a fit of these data by a curve proportional to the water content of the film as estimated from the data in Fig. 6. The excellent agreement between the two sets of data until $t = 132$ s once again points toward a constant number of particles in the irradiated volume.

It is now possible to calculate the values of the film thickness h from the fit of the invariant according to Eqn. (10), which yields the value of the constant K, and then inverting Eqn. (9) to obtain $h\phi_s$:

$$h\phi_s = \frac{K}{2\pi^2 \Delta\rho^2} \tag{11}$$

From the fit we find $K = 1.61 \pm 0.1 \times 10^{-2}$ nm^{-3}. Using the values of ϕ_s determined from the peak position (Fig. 6), we find that the initial thickness of the film ($\phi_s = 0.14$) was $h_{init} = 10.1$ μm, the thickness at $t = 0$, the time of the first spectrum ($\phi_s = 0.16$), was $h_0 = 8.8$ μm and the final thickness of the solid film ($\phi_s = 0.68$), was $h_f = 2.1 \pm 0.2$ μm.

At $t = 132$ s, the integral of the intensity over all scattering vectors increases by a factor of 3.2 ± 0.1, as observed in Figs. 8 and 9. Again, this is interpreted as an increase in contrast, resulting from the intrusion of air into the pore spaces of the film. In the case of three levels of electronic density, ρ_0 (air), ρ_w (water) and ρ_s (silica) the expression of the average fluctuation of the electronic density is (Supplementary Information):

$$\langle \eta^2 \rangle = (\rho_0 - \rho_w)^2 \phi_0 \phi_w + (\rho_w - \rho_s)^2 \phi_w \phi_s + (\rho_s - \rho_0)^2 \phi_s \phi_0 \tag{12}$$

Using the known electronic densities of silica and water, the final silica volume fraction $\phi_s = 0.68 \pm 0.02$, and the relation $\phi_s + \phi_w + \phi_0 = 1$, we can now determine ϕ_0 and ϕ_w through the measured ratio

$$\frac{\langle \eta^2_{dry} \rangle}{\langle \eta^2_{wet} \rangle} = \frac{Q_{dry}}{Q_{wet}} \tag{13}$$

A resolution of Eqns. (12) and (13) with $Q_{dry}/Q_{wet} = 3.2 \pm 0.1$ yields a final air volume fraction $\phi_0 = 0.16 \pm 0.01$ and a water volume fraction $\phi_w = 0.16 \pm 0.01$.

Scattering from cracks

During additional experiments to those described above, the detector distance was increased from 1 m to 10 m, allowing observation of larger features in the films. Scattering patterns could now resolve anisotropic streaks, radiating away from the beam, as shown in Fig. 10. These streaks, suggestive of film cracking, appeared

immediately after the solid volume reached its final packing, and when the transparency of the film changed (as in Fig. 2). The extension of these streaks (to $q = 0.03$ nm^{-1}) indicates that their characteristic size, $1/q$, is approximately 33 nm. At a film thickness of 2.1 μm, this would represent a crack opening strain [29] of at least 0.03. Similar strains were seen by electron microscopy for cracks in fully dried silica. The appearance of cracks at this time confirms that the packed region behaves as a solid, and is capable of transmitting stress.

Observations through the video camera

Images of the whole film were taken throughout the drying process, in order to assess the movement of the drying front with respect to the spot irradiated by the X-ray beam. Initially, the liquid film appeared smooth and transparent. As the film dried, an opaque band grew from the top edge of the film, and descended toward the bottom edge. At the time where the SAXS results indicated that the silica particles had aggregated in the region irradiated by the beam, the images taken by the video camera indicated that the opaque area had reached approximately the same region. Since the SAXS scattering from cracks was observed immediately after the aggregation of silica, we concluded that the scattering of light by the rough surface of the cracked solid film reduced its transparency. By tracking the position of the front of this opaque area, we could thus measure the velocity, v, of the drying front. After a gradual, initial acceleration, this velocity remained within 100 ± 10 μm/s from approximately 50 s onwards, throughout drying. This allows us to convert the information we obtained over time, at one point, into a description of the spatial structure of the travelling drying fronts. For example, noting that aggregation and pore-opening were separated, in time, by 42 s implies that the pore-opening front lagged approximately 4 mm behind the aggregation front.

DISCUSSION

Three transitions

Briefly, we observed three transitions in the structure of a drying colloidal film, as a result of evaporation, and interactions between particles. The initially disperse silica particles first ordered (until $t = 72$ s), then aggregated into a rigid solid (from $t = 72$ s to $t = 90$ s), and then this aggregate structure was infiltrated by air (at $t = 132$ s) (Fig. 11). These changes were expressed as drying fronts, which propagated across the film at some speed v, as have been previously reported [3, 4, 12, 30, 31]. Observing at one point, the transitions were seen as occurring at different times, as the fronts successively passed through the beam. Here, we shall explore the implications of our results, and relate them to the transport processes at work during the drying of a thin colloidal film.

$h\phi_s$ is conserved

The volume of silica per unit area, $h\phi_s$, in the path of the X-ray beam, was conserved throughout the diverse stages of drying. This was established by two independent methods. First, the relative intensity of the high-q scattering signal remained constant throughout drying, until the contrast change introduced by pore-opening. Second, the evolution of the integrated scattered intensity Q agreed with that predicted from the peak position (and hence ϕ_s), on the assumption of a fixed volume of silica in the beam path.

A situation of constant $h\phi_s$ is in sharp contrast to the so-called coffee-ring effect, which involves large-scale transport of solid material towards the edge of a drying dispersion [1, 2, 10, 11]. Our result implies, instead, that there was no net flow of particles into or out of the area irradiated by the beam. Either the particles are immobile, despite any other transport of water, or any particle flow out of this area is compensated for by another flow that keeps the number of particles constant. We will now demonstrate that there was no such flow.

No far-field flow

Sufficiently far ahead of the drying fronts, the film behaves as a still fluid, with evaporation off its surface. We can consider what would be the implications of a far-field flow of speed w in the film, as indicated in Fig. 11. During a short time Δt, a region of the dispersion, of width $\Delta x = v\Delta t$, will have solidified. In addition to the silica initially present in this region, with a volume per unit breadth of $h\phi_s\Delta x$, the flow would also deposit a silica volume of $wh\phi_s\Delta t$. A mass-balance on the solid phase thus implies that a far-field flow would lead to accumulation at the aggregation front, such that

$$h_f\phi_f = h_0\phi_0(1 + w/v) \tag{14}$$

where h_0 and ϕ_0 are the initial height and solid volume fraction, respectively. The high-q limit of $q^4 I_{exp}(q)$, shown in Fig. 8, is proportional to $h\phi_s$. Before aggregation, averaged from 0 to 87 s, this limit is $(2.37 \pm 0.03)\times10^{-3}$ nm^{-4}, while between aggregation and pore opening (averaging 90 to 129 s) it is $(2.32 \pm 0.06)\times10^{-3}$ nm^{-4}. Thus there has been no accumulation at the drying front, and therefore drying does not induce a significant far-field flow (i.e. $w \ll v$) over the lengths of a few mm that occur in this experiment.

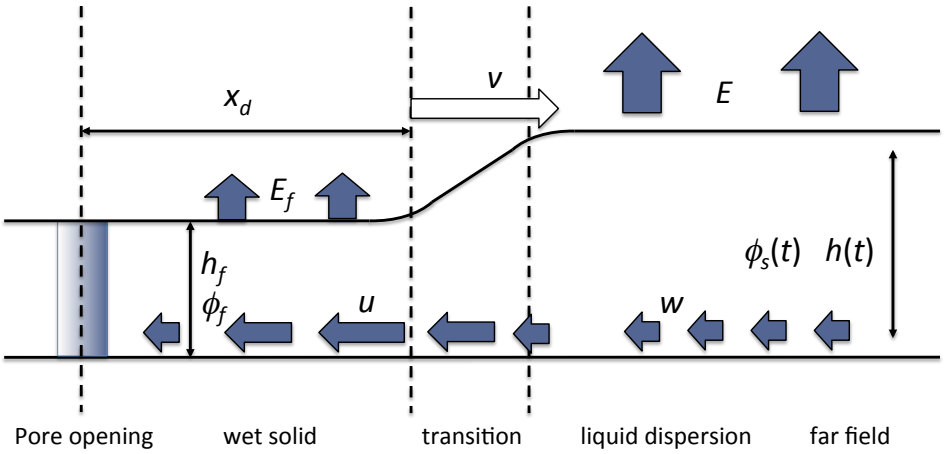

FIG. 11: Sketch of the drying dynamics of a thin colloidal film. As a liquid, the film thickness h and solid volume fraction ϕ_s evolve with time, reaching final values h_f and ϕ_f, respectively, after aggregation. Evaporation over the dispersion, at a rate E, and the wet solid region, at a rate E_f, drives flow in the film. This can generate a far-field velocity w, a dispersant velocity u, and a front velocity v, of the aggregation and pore opening fronts.

The transition region

As it dries, evaporation off the film causes the film thickness h to decrease, and the silica volume fraction, ϕ_s, to rise from 0.14 to 0.68. Consider now a simple model of evaporation with no net flow of either particles, or water, into or out of the area irradiated by the beam. With a constant evaporation rate $E = -dh/dt$, and a constant volume of silica per unit area, $h\phi_s$, we would predict

$$Et = h_0 - h(t) = h_0 - \frac{h_0\phi_0}{\phi_s(t)} \tag{15}$$

The data for ϕ_s are re-plotted in Fig. 12 against this prediction. For the first 50 s, water is removed at a constant evaporation rate of 60 ± 6 nm/s. This is of the same order as a typical value of 3 mm/day = 35 nm/s for evaporation off pure, still water at room temperature and ambient humidity [9]. After this point, however, there are systematic deviations, which indicate that water is being drawn out of the irradiated area at a faster rate, prior to solidification at 90 s. It is only in this limited transition region that drying and transport are affected by the directional drying fronts.

Within the transition region water is being drawn out at an increased rate, through capillary suction, ultimately to balance evaporation over the wet solid film. This can be accounted for by allowing the water phase to take a superficial fluid speed (or volume flux) of $u(x,t)$, while continuing to assume no net movement of the silica particles, which have reduced mobility due to their repulsions and high volume fraction ($\phi_s > 0.35$). The mass balance at the point of the beam is now

$$\frac{dh}{dt} = -E + \frac{d(uh)}{dx} \tag{16}$$

where the additional term accounts for height changes caused by flow of water out of the region, and the positive sign accounts for the difference in direction between the flow u, and the motion of the drying front, v. Relying on the relation $v = dx/dt$, and assuming that u is initially zero, integration of Eqn. (16) yields

$$Et = h_0 - \frac{h_0\phi_0}{\phi}\left(1 - \frac{u}{v}\right) \tag{17}$$

Fig. 12(b) shows the ratio u/v inferred from this model. The water accelerated from rest to approximately 0.45 of the front speed, at the point of solidification. The error on this ratio is considerable, and cannot be estimated rigorously with the given data, but a range of ± 0.15 is likely to be sufficiently conservative. The influence of the drying front decays away quickly, with a characteristic length-scale of the transition region of order 1 mm.

At this point we remark that we can define the transition region according both local and non-local criteria. From a non-local point of view, it is the region where deviations from Eqn. (15) occur, and therefore where the height and volume fraction of the film are not uniform (outside this region, they are). The gradient in volume fraction is associated with a gradient in osmotic pressure. This gradient compensates for the drag force created by the capillary suction and allows the movement of the fluid to become different from that of the particles.

This situation is quite similar to the formation of a polarization region in dead-end filtration [32, 33]. The difference with dead-end filtration is that, since $h\phi_s$ re-

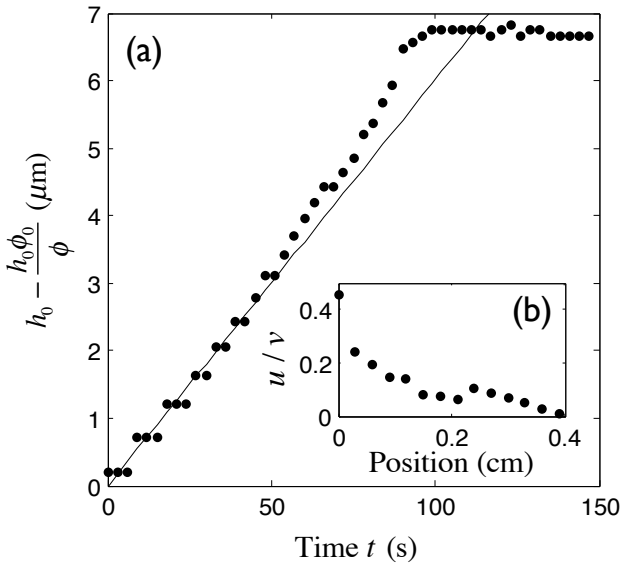

FIG. 12: The evolution of the silica volume fraction (see Fig. 6) reveals transport mechanisms. For a constant evaporation rate, and volume of silica per unit surface area, the film height should vary linearly with time, as shown by the straight line, which has been fitted to early-time data. Deviations occur near the aggregation front, which can be used (insert) to determine the ratio of the water velocity u to the front speed v. Here, positions are calculated using $v = 100$ μm/s, with aggregation occurring at 90 s.

mains constant, this higher volume fraction is compensated by a lower thickness h. Thus the transition region can be visualized as a polarization wave that travels ahead of the drying front. In a travelling wave, where the total number of particles in the transition region is constant (although particles will be both entering, and leaving), there is no accumulation. This leads to the formation of a homogeneous film, as in the present case. If the transition region is growing (as near the film edge), or shrinking (as near the center of the film, or when it meets some barrier), accumulation/coffee-ring behavior can occur, and the natural length scale over which this behavior is expressed will then be the width of the transition region.

From a local point of view, the transition region is the region where the evolution of the first peak of the structure factor (Figs. 5 and 7) shows that the particles have been jammed by the compaction [27] into a structure with low short-range order, presumably consisting of limited aggregates [26, 28]. The volume fraction where this occurs ($\phi_s = 0.35$) is the same where bulk samples with the same interparticle repulsions turn to a gel-like rheology. The cause of this extra compaction is, of course, the flow of water into the wet solid, and this is where the two descriptions (local and non-local) meet.

The solid film

After 90 s the dispersion had aggregated into a wet solid, and the position and height of the peak in the structure factor $S(q)$ remained constant, indicating a final volume fraction $\phi_s = 0.68 \pm 0.02$. This is higher than the expected volume fraction of 0.64 for a random close packing of mono-disperse spheres, which may be either the result of a broad size-distribution or some residual short-range ordering of the particles. However, the uncertainty on this measurement remains too large to make further conclusions about the inter-particle structure.

Immediately after aggregation, we observed cracking. This demonstrates that the film surface is being stressed, that the particle packing is capable of transmitting that stress, and that the stresses are not otherwise rapidly relaxed. In this case, it is typically argued that the particles are in intimate (van der Waals-dominated) contact with each other, with surface stresses generated by capillary forces, acting on the curved menisci between particles at the film-air surface [3, 9, 30]. The strain relieved by cracking was not large, approximately 0.03, but this behavior is consistent with prior observations of drying silica dispersions [3, 4, 34, 35].

The film remained as a wet solid from 90 to 132 s, a period of $\tau_d = 42 \pm 3$ s. This was indicated by the constant high-q limit of the scattered intensity, and the invariant, Q, during this time. However, evaporation continued off this wet solid, at a rate E_f, balanced by a flow of water through the porous particle network, as sketched in Fig. 11. The superficial fluid velocity should take a maximum, u_0, at the aggregation front, and decrease slowly until stagnation at the pore opening front, over a distance, $x_d = v\tau_d$. Assuming that x_d is constant, then this mass balance is simply [12]

$$u_0 = \frac{E_f x_d}{h_f} \tag{18}$$

from which we can evaluate the evaporation rate over the wet solid region, and compare it to that over the liquid film. Using $h_f = 2.1 \pm 0.2$ μm, $\tau_d = 42\pm 3$ s, and a ratio of velocities $u_0/v = 0.45 \pm 0.15$, we find an average evaporation rate of $E_f = 23 \pm 8$ nm/s. Despite the considerable uncertainties here, this is significantly lower than the evaporation rate of the liquid film. It is possible that, as the particle network now covers the majority of the exposed surface, evaporation on the wet aggregated film is reduced, for example by a factor of $1 - \phi_s$, below that over the liquid dispersion.

In the final stage of drying, air percolates into the film, accessing the pore spaces between neighboring particles. This was observed by a change in scattering contrast. This transition appears to have a finite width, although it is close to our experimental resolution. A considerable fraction of water, 0.16 ± 0.01, was found to remain in the

apparently dry state, after pore opening was complete. This residual water content corresponds to a water layer thickness of 0.6 nm for densely packed spheres of radius 8.15 nm. This amount of residual water is close to the expected water layer thickness on silica (1 nm at RH = 50 %) [36].

CONCLUSIONS

The full sequence of drying that we have described here is similar to other reports of drying colloidal films [3, 4, 12, 28, 31] and extends the applicability of these ideas into the very thin ($\sim$ 1-10 μm) dip-coating limit. Moreover, it provides some answers to the questions raised in the introduction:

(1) The SAXS experiments show that the number of particles at any given spot in the liquid film is conserved throughout the drying process. Therefore, at large distances from the liquid-solid boundary, the film is still, and there is no far-field flow. Yet, near this boundary, there must be a flow of the liquid phase into the wet solid.

(2) We find that the number of particles at any given location is conserved before, during and after the crossing of the aggregation front. Still, the capillary suction in the wet solid creates a local flow in a transition region near the liquid/solid boundary. In this region, a balance between osmotic pressure, flow and evaporation rate could explain the conservation of the number of particles despite the flow.

(3) In very thin films containing repelling particles, the normal evaporation causes the particle volume fraction to rise progressively. As the aggregation front approaches the point of measurement, the flow of water toward the wet solid film accelerates the compaction of the particles. At the end of this transition region, the volume fraction reaches that of a random dense packing of these particles at the liquidsolid boundary (0.68).

(4) In our experiment, the film behaves as a solid from the time that aggregation is complete, as indicated by the coincidence between the onset of cracking and the time when the maximum silica volume fraction is reached. However, it seems that aggregation starts significantly sooner, suggesting that solidification takes place by the growth of small clusters of aggregated particles. The solid is dense, but it has a low degree of short-range order. This may be due to the aggregation process and to the size distribution of the particles.

(5) The evaporation rate over the solid film is about one-third that over the liquid film. This may be due to the fraction of surface area that is obstructed by the particles. This evaporation from the wet solid is contrast to the case of the coffee-stain evaporation pattern. Indeed, when the liquid film is not surrounded by a wet solid, the evaporation rate diverges near the boundary of the liquid [1, 2, 7]. In the present case there is also an excess loss of liquid at the boundary of the liquid, but it is due to evaporation from the wet solid.

The information available in (1)-(5) characterizes the drying process in the case of homogeneous film formation (hϕ_s constant, implying conservation of the number of particles in any given spot). The same type of experiments could be performed on different films that are more susceptible to far-field flows: films of liquid dispersions with a lower particle concentration, or with weaker interparticle repulsions, or thicker films. Crossing over to the coffee-stain mechanism would make it possible to quantify the respective role of the different parameters and predict which deposits will evolve to the formation of a homogenous solid film, and which ones will show macroscopic transport.

ACKNOWLEDGMENTS

We thank P. Bacchin, D. Bartolo, S. Herminghaus, B. Jönsson, V. Nikolayev, D. Quéré, and H. Wennerström for enlightening discussions, ESRF for making beamtime and instruments available to us, F. Pignon and K. Roger for sharing some of their beam-time allocations, ANR for financial support (CRUNCH:ANR-BLAN06-3-144450).

* lucas.goehring@ds.mpg.de

[1] Deegan, R. D.; Bakajin, O.; Dupont, T. F.; Huber, G.; Nagel, S. R.; Witten, T. A. *Nature* **1997**, *389*, 827–829.
[2] Deegan, R. D.; Bakajin, O.; Dupont, T. F.; Huber, G.; Nagel, S. R.; Witten, T. A. *Phys. Rev. E* **2000**, *62*, 756–765.
[3] Dufresne, E. R.; Corwin, E. I.; Greenblatt, N. A.; Ashmore, J.; Wang, D. Y.; Dinsmore, A. D.; Cheng, J. X.; Xie, X. S.; Hutchinson, J. W.; Weitz, D. A. *Phys. Rev. Lett.* **2003**, *91*, 224501.
[4] Dufresne, E. R.; Stark, D. J.; Greenblatt, N. A.; Cheng, J. X.; Hutchinson, J. W.; Mahadevan, L.; Weitz, D. A. *Langmuir* **2006**, *22*, 7144.
[5] Harris, D. J.; Hu, H.; Conrad, J. C.; Lewis, J. A. *Phys. Rev. Lett.* **2007**, *98*, 148301.
[6] Harris, D. J.; Lewis, J. A. *Langmuir* **2008**, *24*, 3681–3685.
[7] Berteloot, G.; Pham, C.-T.; Daerr, A.; Lequeux, F.; Limat, L. *Europhys. Lett.* **2008**, *83*, 14003.
[8] Parneix, C.; Vandoolaeghe, P.; Nikolayev, V. S.; Quéré, D.; Li, J.; Cabane, B. *Phys. Rev. Lett.* **2010**, *105*, 266103.
[9] Routh, A. F.; Russel, W. B. *AIChE J.* **1998**, *44*, 2088–2098.
[10] Marín, A. G.; Gelderblom, H.; Lohse, D.; Snoeijer, J. H. *Phys. Rev. Lett.* **2011**, *107*, 085502.
[11] Yunker, P. J.; Still, T.; Lohr, M. A.; Yodh, A. G. *Nature* **2011**, *476*, 308–311.
[12] Goehring, L.; Clegg, W. J.; Routh, A. F. *Langmuir* **2010**, *26*, 9269–9275.

[13] Gundabala, V. R.; Lei, C. H.; Ouzineb, K.; Dupont, O.; Keddie, J. L.; Routh, A. F. *AICHE J.* **2008**, *54*, 3092–3105.

[14] Sarkar, A.; Tirumkudulu, M. S. *Langmuir* **2009**, *25*, 4945–4953.

[15] Jönsson, B.; Persello, J.; Li, J.; Cabane, B. *Langmuir* **2011**, *27*, 6606–6614.

[16] Spalla, O. In *Neutrons, X-rays and light: scattering methods applied to soft condensed matter*; Lindner, P., Zemb, T., Eds.; North Holland Press, 2002; Chapter 3.

[17] Glatter, O.; Kratky, O. *Small Angle X-ray Scattering*; Academic Press: New York, 1982; p 515.

[18] Hiltner, P. A.; Papir, Y. S.; Krieger, I. M. *J. Phys. Chem.* **1971**, *75*, 1881.

[19] Goodwin, J. W.; Ottewill, R. H.; Parentich, A. *J. Phys. Chem.* **1980**, *84*, 1580–1586.

[20] Spalla, O.; Nabavi, M.; Minter, J.; Cabane, B. *Colloid Polym. Sci.* **1996**, *274*, 555–567.

[21] Cebula, D. J.; Goodwin, J. W.; Jeffrey, G. C.; Ottewill, R. H.; Parentich, A.; Richardson, R. A. *Faraday Discuss.* **1983**, *76*, 37–52.

[22] Hayter, J. B. *Farad. Discuss. Chem. Soc.* **1983**, *76*, 7–17.

[23] Härtl, W.; Versmold, H. *J. Chem. Phys.* **1988**, *88*, 7157–7161.

[24] Pusey, P. N. In *Liquids, Freezing, and Glass Transition*; Hansen, J. P., Levesque, D., Zinn-Justin, J., Eds.; North Holland Press, 1989; Chapter 10.

[25] Versmold, H.; Wittig, U.; Hartl, W. *J. Phys. Chem.* **1991**, *95*, 9937–9940.

[26] Cardinaux, F.; Stradner, A.; Schurtenberger, P.; Sciortino, F.; Zaccareli, E. *Europhys. Lett.* **2007**, *77*, 48004.

[27] Jacquin, H.; Berthier, L. *Soft Matter* **2010**, *6*, 2970–2974.

[28] Cardinaux, F.; Zaccarelli, E.; Stradner, A.; Bucciarelli, S.; Farago, B.; Egelhaaf, S.; Sciortino, F.; Schurtenberger, P. *J. Phys. Chem. B* **2011**, *115*, 7227–7237.

[29] J. L. Beuth Jr., *Int. J. Solids Structures* **1992**, *29*, 1657–1675.

[30] Chiu, R. C.; Garino, T. J.; Cima, M. J. *J. Am. Ceram. Soc.* **1993**, *76*, 2257–64.

[31] Allain, C.; Limat, L. *Phys. Rev. Lett.* **1995**, *74*, 2981–2984.

[32] Jönsson, A. S.; Jönsson, B. *J. Colloid Interface Sci.* **1996**, *180*, 504–518.

[33] Bacchin, P.; Si-Hassen, D.; Starov, V.; Clifton, M. J.; Aimar, P. *Chem. Eng. Sci.* **2002**, *75*, 77–91.

[34] Lazarus, V.; Pauchard, L. *Soft Matter* **2011**, *7*, 2552–2559.

[35] Gauthier, G.; Lazarus, V.; Pauchard, L. *Langmuir* **2007**, *23*, 4715–4718.

[36] Asay, D. B.; Kim, S. H. *J. Phys. Chem. B* **2005**, *109*, 16760–16763.

Supplementary information for:
"Drying dip-coated colloidal films"

Joaquim Li, Bernard Cabane, Michael Sztucki, Jérémie Gummel, Lucas Goehring

Calibration of the peak positions

In order to calibrate the relation between the position of the peak in the structure factor q_{peak} and the silica volume fraction ϕ_s, we used a series of dispersions obtained through dialysis with aqueous solutions of PEG 35000 (see Materials and Methods). We measured q_{peak} and ϕ_s in each one. This calibration does not depend on any assumptions regarding the sizes or the ordering of the silica particles, provided that the short-range order is determined by ϕ_s only. We then found that $(q_{peak})^3$ is proportional to ϕ_s, in the range (0.03 – 0.5), as it should for repelling particles (Figure SI-1) [1]. Moreover, this relation of proportionality can be modelled by treating the system as a face-centered cubic array of particles with a number-averaged radius R_p = 8.15 nm [1]

$$\left(q_{peak}\right)^3 = \left(\frac{2\pi}{d_{111}}\right)^3 = \frac{36\pi^2\sqrt{3}}{\left(2R_p\right)^3}\phi_s \text{ with } \quad d_{111} = \left(\frac{16\pi}{3\phi_s}\right)^{1/3}\frac{R_p}{\sqrt{3}} \qquad \text{/SI-1/}$$

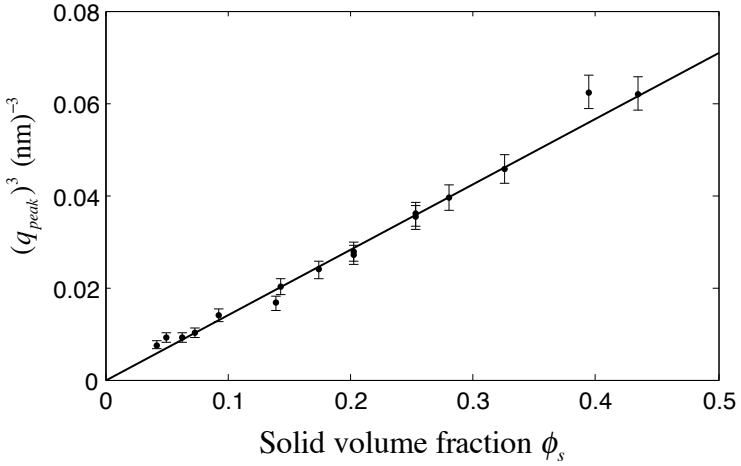

Figure SI-1. The relation between the position of the first peak of the structure factor and the volume fraction of silica particles in the dispersion. Two series of concentrated dispersions were prepared separately, and both gave the same calibration curve, with a coefficient of proportionality of 0.142 ± 0.03 nm^{-3}, as shown.

Determination of the integral of the scattered intensity

At high q values, the integral of the intensity scattered in all directions of reciprocal space goes to a limit (Qh) that depends only on the average fluctuation of the density of scattering length in the volume that is irradiated by the beam. For materials that have only 2 levels of the density of scattering length, this average fluctuation is expressed simply as a function of this difference in scattering density, and of the volume fraction of these two phases

$$Qh = \int_0^\infty I_{exp}(q)\, q^2 dq = 2\pi^2 h \phi_s \Delta\rho^2 \left(1-\phi_s\right) \qquad \text{/SI-2/}$$

The SAXS experiment does not reach infinite q values; therefore, we have measured the values of Qh at finite q_{max} values. Fig. SI-2 shows how Qh varies with q_{max} for a selection of spectra recorded during the drying of a film. We see that, due to the low signal / noise ratio at high q, the value of Qh fluctuates considerably for values of q_{max} that are beyond 3 nm^{-1}. Such q values correspond to distances below 3 nm, which are intra- rather than inter-particle distances. We take advantage of this fact to overcome the signal/noise problem.

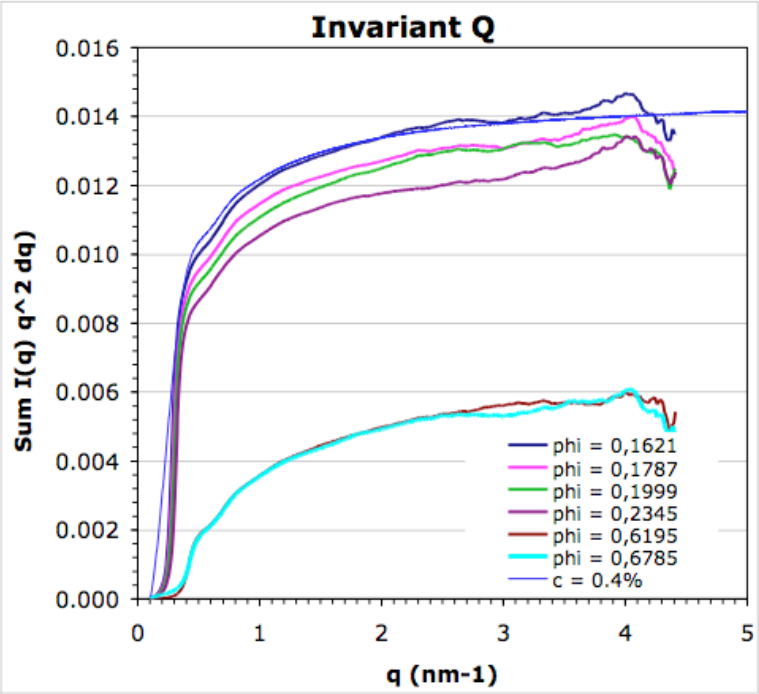

Figure SI-2. The integral of the scattered intensity of the film as a function of the highest value of q used for the integration. The line that extends beyond q = 4.5 nm^{-1} is the corresponding integral for a dilute dispersion, using a scale factor that matches both sets of data at q = 3 nm^{-1}.

In order to obtain more accurate values of Qh, we used a spectrum recorded independently for a thick (h = 1 mm) sample of a dilute ($\phi_s = 4 \times 10^{-3}$) dispersion of the same colloidal silica. For this spectrum, we had a better signal over noise ratio that allowed us to calculate an accurate value of Qh, taking q_{max} = 5 nm^{-1} (Fig. SI-3). We note that the asymptotic limit of the scattering from the dilute dispersion is approximately 10% higher than that of polydisperse spheres with the same average radius (Fig. SI-3). This is because the individual silica particles have non-spherical surfaces, as shown by transmission electron microscopy [2].

Since the particles in the dilute dispersions and those in the films were the same, and since they are incompressible, we spliced the data from a dilute dispersion and from the films to obtain SAXS curves that matched the film data at all q values corresponding to inter-particle distances (q < 3 nm^{-1}) but had better signal ratio for distances that were well within a particle (q> 3 nm^{-1}). These spliced curves were then used to calculate the value of Qh.

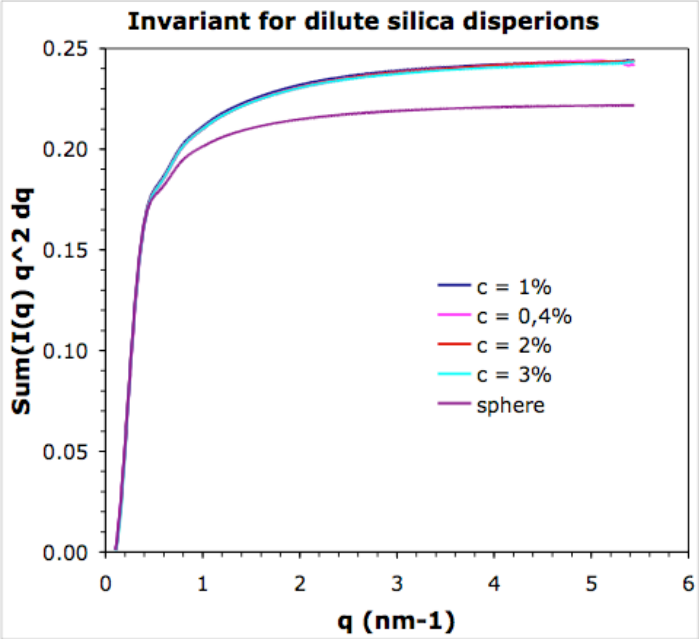

Figure SI-3. The integral of the scattered intensity as a function of the highest value of q used in the integration, for dilute dispersions of Ludox HS-40 colloidal silica, compared with the theoretical limit for polydisperse spheres with a Schulz distribution of radii, as defined in the main text, Fig. 4. All intensities have been normalized to that given by a dispersion of concentration $\phi_s = 1 \times 10^{-2}$.

Determination of the Porod limit of the scattered intensity

At high q values, materials that have only two levels of the density of scattering length follow Porod's law, which is a q^{-4} decay of the intensity. The prefactor of this power law, also called the Porod limit, is determined by the total area of interface between the two phases of the material, as expressed in Eqn. /SI-3/ (corresponding to Eqn. /6/ of the main text).

$$\lim_{q\to\infty} q^4 I_{exp}(q) = 2\pi h \phi_s \Delta\rho^2 \frac{A_p}{V_p} \qquad \text{/SI-3/}$$

In order to determine this limit, we used the classical plot of $I(q)$ vs. q^{-4}: the prefactor of the power law is the initial slope of this plot, and the ordinate at the origin is a background correction.

Fig. SI-4 shows an example of this type of plot for a thick sample (h = 1 mm) of a dilute dispersion of the same colloidal silica ($\phi_s = 4 \times 10^{-3}$). These plots are compared with the theoretical plot for a Schulz distribution of spheres with a mean radius R_p = 8.0 nm and width σ_R/R_p=0.14. As seen in Fig. SI-2, the Porod limit of the Ludox HS-40 particles is higher than that of the corresponding spheres, because the particles are somewhat aspherical.

Using the plot shown in Fig. SI-4, which yields a Porod limit $q^4 I(q) = 1.68 \times 10^{34}$ m^{-4}, together with Qh for the same dispersion, $Qh = 8.91 \times 10^{25}$ m, a difference in density of scattering length $\Delta\rho^2 = 5.69 \times 10^{29}$ m^{-2}, and a volume fraction $\phi_s = 4 \times 10^{-3}$, we obtained a surface area per unit volume $A_p/V_p = 5.90 \times 10^8$ m^{-1} through Eqn. SI-4:

$$\frac{\lim_{q\to\infty} q^4 I_{exp}(q)}{Qh} = \frac{A_p}{V_p} \times \frac{1}{\pi(1-\phi_s)} \qquad \text{/SI-4/}$$

This surface area per unit volume corresponds to an area per unit mass $A_p/M_p = 2.68 \times 10^5$ m^2kg^{-1}, slightly higher than that provided by the manufacturer from BET measurements ($A_p/M_p = 2.20 \times 10^5$ m^2kg^{-1}).

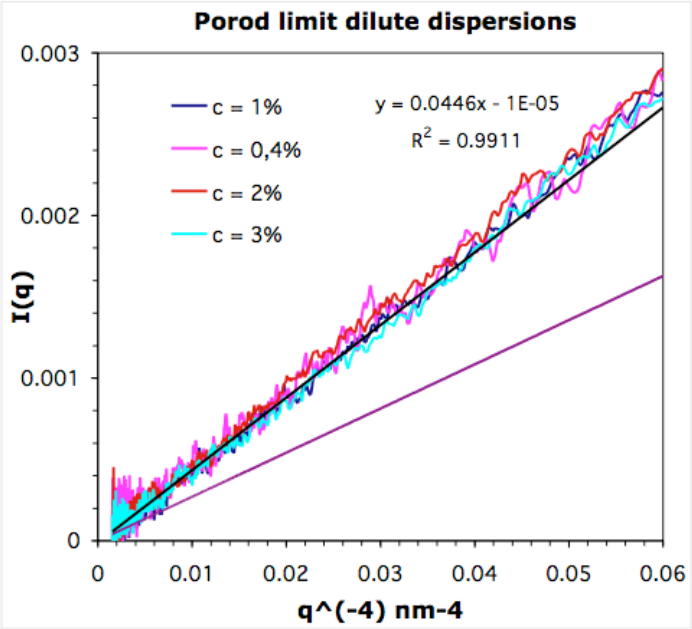

Figure SI-4. The Porod limit of dilute dispersions of Ludox HS-40 colloidal silica, compared with the theoretical limit for a Schulz distribution of spheres with the same average radius. All intensities have been normalized to that given by a dispersion of concentration $\phi_s = 1 \times 10^{-2}$.

Fig. SI-5 shows the Porod plots for a selection of spectra recorded during the film drying experiment. Because these spectra have a low signal-to-noise ratio at high q, the accuracy on the initial slope on the Porod plots is poor. Consequently, we have determined this slope using an extended range of q (from q = 1.2 to 3.2 nm^{-1}). This results in systematically underestimated slopes. As in the case of the invariant, we can use the comparison with the scattering from bulk samples to evaluate the required correction.

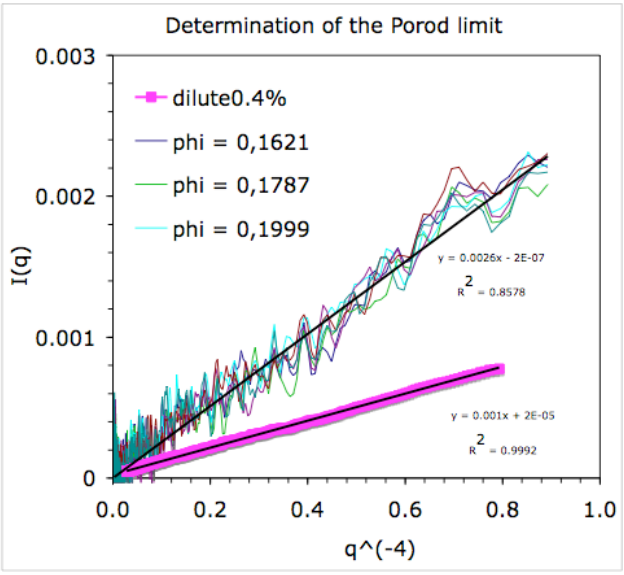

Figure SI-5. The Porod limit of dilute films of Ludox HS-40 colloidal silica, compared with that for dilute dispersions of the same colloidal silica.

Indeed, the distances probed by the experiment in this range of q values extend from $d = 2\pi/q$ = 2 to 5 nm. These distances are essentially intraparticle rather than interparticle distances. Accordingly, we assumed that the variations of the Porod limit at very high q values were the same for the drying films and for bulk samples of dilute silica dispersions. The slopes of the Porod plots given in Fig. SI-6 shows that this is true within experimental uncertainties. Accordingly, based on the evolution of the slope of the Porod plot with changes in the q^{-4} range used, the Porod limit determined for films in the range extending to $q^{-4} = 0.5$ nm^4 was only 80 % of the true asymptotic Porod limit (asymptotic value 2.9×10^{-3} nm^{-4} rather than 2.35×10^{-3} as seen in Fig. 8 of the main text).

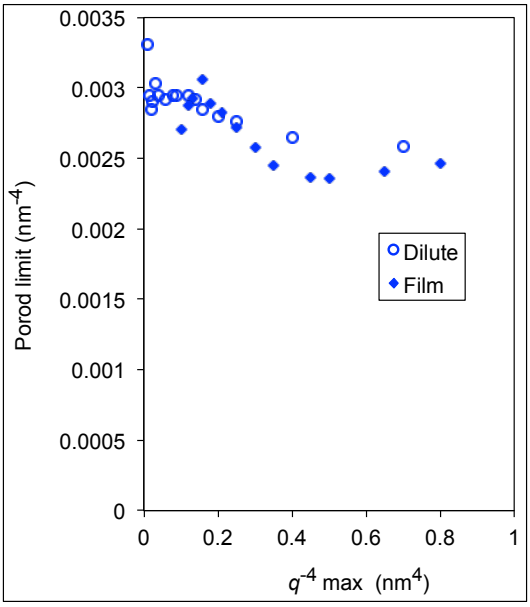

Figure SI-6. Evolution of the initial slope of the Porod plot depending on the q range considered for the determination of the slope. Horizontal scale: highest value of q^{-4} used in the determination of the slope of the Porod plot. Full diamonds are the data obtained for a thick sample of a dilute dispersion of ludox HS-40 colloidal silica, scaled to match the average level of the film data. Empty circles are an average over time of the data obtained for the spectra recorded during the drying film experiment.

Agreement between the absolute values of the volume fraction, Porod limit and the integral of the scattered intensity

One can obtain values of $h\phi_s$ from the fit of the evolution of Qh by Eqn. /11/ in the main text

$$h\phi_s = \frac{K}{2\pi^2 \Delta\rho^2} \qquad /SI\text{-}5/$$

as well as the from the value of the Porod limit

$$h\phi_s = \frac{\lim_{q\to\infty} q^4 I_{\exp}(q)}{2\pi\Delta\rho^2 \frac{A_p}{V_p}} \qquad /SI\text{-}6/$$

By combining Eqns. SI-5 and SI-6 we obtain

$$\lim_{q\to\infty} q^4 I_{\exp}(q) = \frac{K}{\pi}\frac{A_p}{V_p} \qquad /SI\text{-}7/$$

In order to check the consistency of our measurements, we need an estimate of the ratio A_p/V_p. Such a ratio has been obtained from Eqn. SI-4. We obtained $A_p/V_p = 5.90 \times 10^8$ m^{-1}. Using this value for A_p/V_p and $K = 1.61 \times 10^{-2}$ nm^{-3} one finds a Porod limit of 3.0×10^{-3} nm^{-4}. This is in agreement with the trends shown in Fig. SI-6.

The integral of the scattered intensity for systems with either 2 or 3 constant levels of scattering density

Consider a material described by its electronic density, $\rho(\vec{r})$. This density has an average value, $\langle\rho(\vec{r})\rangle$, and its spatial fluctuations around the average value are described by $\eta(\vec{r})$:

$$\eta(\vec{r}) = \rho(\vec{r}) - \langle\rho(\vec{r})\rangle \qquad \text{/SI-8/}$$

The scattered amplitude is a Fourier transform of $\eta(\vec{r})$, and the scattered intensity is proportional to the average squared fluctuation $\langle\eta^2(\vec{r})\rangle$. The integral over all $\vec{q}$ vectors of the scattered intensity (also called the invariant) is [3,4]:

$$Qh = \int_0^\infty I_{exp}(q)\, q^2\, dq = 2\pi^2 h \langle\eta^2\rangle \qquad \text{/SI-9/}$$

In a system with only 2 levels of electron density, with some volume fraction ϕ_w of water with an electron density ρ_w, and volume fraction ϕ_s of silica with an electron density ρ_s, the average density $\rho(\vec{r}) = \rho_w\phi_w + \rho_s\phi_s$. In regions of water, the squared fluctuation is

$$\eta_w^2 = (\rho_w - (\rho_w\phi_w + \rho_s\phi_s))^2 \qquad \text{/SI-10/}$$

with a similar expression for η_s^2. The average squared fluctuation is the sum of the squared fluctuations in both types of regions, $\langle\eta_{wet}^2\rangle = \eta_w^2\phi_w + \eta_s^2\phi_s$, which simplifies to the classical expression

$$\langle\eta_{wet}^2\rangle = (\rho_w - \rho_s)^2\,\phi_w\phi_s = (\rho_w - \rho_s)^2\,\phi_s(1-\phi_s) \qquad \text{/SI-11/}$$

For a three-phase system, if some regions are filled with air of an electron density ρ_0, and volume fraction ϕ_0, the new total average electron density is $\langle\rho(\vec{r})\rangle = \rho_0\phi_0 + \rho_w\phi_w + \rho_s\phi_s$, and thus, for example,

$$\eta_w^2(\vec{r}) = \left[\rho_w(\vec{r}) - (\rho_0\phi_0 + \rho_w\phi_w + \rho_s\phi_s)\right]^2 \qquad \text{/SI-12/}$$

The average squared fluctuation is now the sum of the squared fluctuations in all 3 types of regions:

$$\langle\eta_{dry}^2\rangle = \eta_0^2\phi_0 + \eta_w^2\phi_w + \eta_s^2\phi_s$$

$$= \rho_0^2\phi_0(\phi_w+\phi_s) + \rho_w^2\phi_w(\phi_0+\phi_s) + \rho_s^2\phi_s(\phi_0+\phi_w) - 2\rho_0\rho_w\phi_0\phi_w - 2\rho_0\rho_s\phi_0\phi_s - 2\rho_w\rho_s\phi_w\phi_s \qquad \text{/SI-13/}$$

which simplifies to

$$\langle\eta_{dry}^2\rangle = (\rho_0 - \rho_w)^2\,\phi_0\phi_w + (\rho_w - \rho_s)^2\,\phi_w\phi_s + (\rho_s - \rho_0)^2\,\phi_s\phi_0 \qquad \text{/SI-14/}$$

We have measured the integral of the scattered intensity in the wet and in the dry solid. Therefore we can determine ϕ_w and ϕ_0 through the ratio

$$\frac{\langle \eta_{dry}^2 \rangle}{\langle \eta_{wet}^2 \rangle} = \frac{Q_{dry}}{Q_{wet}} \qquad \text{/SI-15/}$$

and the relation $\phi_w + \phi_s + \phi_0 = 1$. A resolution of Equation /SI-15/ with $(\rho_w - \rho_s)^2 = 5.69 \times 10^{29}$, $(\rho_s - \rho_0)^2 = 2.88 \times 10^{30}$, $(\rho_w - \rho_0)^2 = 8.89 \times 10^{29}$, $\phi_2 = 0.68$ and $Q_{dry}/Q_{wet} = 3.2$ yields an air volume fraction $\phi_0 = 0.16$ and a water volume fraction $\phi_w = 0.16$. This residual water content corresponds to 1-2 molecular layers of water on the silica particles, assuming that a dense molecular layer of water has a thickness of 0.3×10^{-9} m. This amount of residual water is what is expected at ambient relative humidity (RH = 50 %) [5].

Final film thickness

In order to find out whether the drying process produced uniform solid films, we performed a SAXS scan of a fully dried dip-coating film along its length (i.e. along the dip-coating direction). Figure SI-7 presents the measured values of the invariant of the scattered intensity and the values of the silica volume fraction, calculated from the position of the first peak of the structure factor. The values of the invariant have been scaled by a constant factor (1/21) in order to facilitate the comparison with the silica volume fraction. Both sets of data indicate that the film is nearly uniform, with a variation of 5% over the central part of the film (positions 5000 to 15000 µm). However, there are significant excesses of deposited silica at both ends of the film, particularly at the bottom end where a bulge of liquid dispersion remained at the end of the dip-coating. We can also note an increase in silica volume fraction at the bulges [6].

After the SAXS experiment was completed, we scanned the film again, using a white light reflectometer to determine the film thickness. For this determination we used the index of refraction of mica (approximated by that of BK7 glass), and that of water. This scan confirmed that the film thickness was uniform, excepted for the bulges at both ends of the film (Figure SI-7). The average film thickness measured in this way (taking the mean value between position 5 mm and 15 mm) was $h = 1.6$ µm, compared with that determined through the SAXS invariant, which was $h = 2.1$ µm

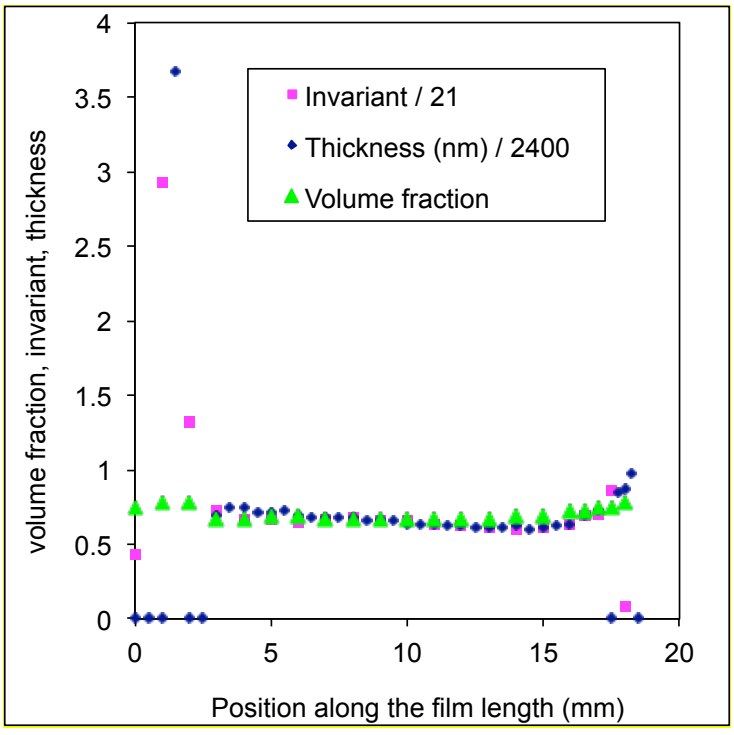

Figure SI-7. Scans through a dry film, along the direction of dip-coating. The horizontal scale goes from 0 (top of the deposited film) to 20 mm (bottom of the mica). Green triangles: Volume fraction of silica, calculated from the position of the first peak of the structure factor. Pink squares: invariant of the scattered intensity, in nm^{-3}, scaled by 1/21. Blue diamonds: thickness of the film, in µm, scaled by 1/2.4. The average film thickness was 2 µm.

References

1 Goodwin, J.W.; Ottewill, R.H.; Parentich, A. *J. Phys. Chem*. **1980**, *84*, 1580.

2 Madeline, J. B.; Meireles, M.; Bourgerette, C.; Botet, R.; Schweins, R.; Cabane, B. *Langmuir* **23**, 1645, (2007).

3 Spalla, O. in *Neutrons, X-rays and light: scattering methods applied to soft condensed matter*; chapter 3, P. Lindner and T. Zemb Eds., North Holland **2002**.

4 Glatter, O.; Kratky, O. *Small Angle X-ray scattering*; Academic Press: London 1982.

5 Asay, D.B. ; Kim, S.H. *J. Phys. Chem. B* **2005**, *109*, 16760

6 Marin, A.G. ; Gelderblom, H. ; Lohse, D. ; Snoeijer, J.H. *Phys. Rev. Lett.* **2011**, 107, 085502